http://dx.doi.org/10.1016/j.optlastec.2020.106374

Micro selective laser melting of NiTi shape memory alloy: Defects, microstructures and thermal/mechanical properties

Jin Fu[a], Zhiheng Hu[b], Xu Song[c,*], Wei Zhai[d], Yu Long[e], Heng Li[f], Mingwang Fu[a,**]

[a] Department of Mechanical Engineering, The Hong Kong Polytechnic University, Hung Hom, Kowloon, Hong Kong

[b] Singapore Institute of Manufacturing Technology (SIMTech), Agency for Science, Technology and Research (A∗STAR), 73 Nanyang Drive, Singapore 637662, Singapore

[c] Department of Mechanical and Automation Engineering, Chinese University of Hong Kong, Shatin, Hong Kong

[d] Department of Mechanical Engineering, National University of Singapore, 9 Engineering Drive 1, Singapore 117575, Singapore

[e] Han's Laser Group, No.9988 Shennan Avenue, Nanshan District, Shenzhen 518057, China

[f] State Key Laboratory of Solidification Processing, School of Materials Science and Engineering, Northwestern Polytechnical University, Xi'an 710072, China

[*] Corresponding author.

[**] Corresponding author.

Email address: xsong@cuhk.edu.hk (Xu Song), mmmwfu@polyu.edu.hk (M.W. Fu).

Abstract

The use of micro selective laser melting (μ-SLM) enables product miniaturization, which is one of the megatrends in the metal processing industry and increasingly find its applications in biomedical and electronics industries. Among these, NiTi shape memory alloy (SMA) shows a great promise in functional micro-scaled components such as stent. There are inevitably some imperfections in SLM, but the imperfection formation in μ-SLM may not be the same as that in the conventional SLM. This work studies the imperfections in μ-SLM produced NiTi samples, with focus on defects, microstructure and thermal/mechanical behaviors. The effects of substrate material, laser-related process parameter and scanning strategy on defects such as porosity and cracks were analyzed, and a process window for "Scanning speed – Hatch spacing" was determined. Transformation peak was hardly detected in thermal behavior of as-printed and post heat-treated μ-SLM NiTi, resulting from microstructure inhomogeneity, Ti-rich impurity phases $TiC_{1-x}N_x$/$Ti_4Ni_2O_x$ and precipitate Ti_2Ni,

which were introduced by powder preparation, μ-SLM or post heat treatment. The as-printed NiTi shows higher compressive strength and fracture strain than the post heat-treated samples, reaching 2796.3 MPa and 28.4% on average, respectively, but the plateau stress-strain stage is indistinguishable due to inhomogeneous and localized stress-induced martensite transformation. The brittle Ti_2Ni phase was introduced in post heat treatment, leading to inhomogeneous microstructure and lower ductility. The underlying mechanisms revealed in these imperfections could serve as a guideline for defect control, process optimization, as well as post heat treatment methods for μ-SLM of NiTi alloy.

Keywords: Micro selective laser melting; Shape memory alloy; Defects; Microstructure; Thermal/mechanical behaviors

1. Introduction

NiTi shape memory alloy (SMA), has been widely used in biomedical and aerospace industries thanks to its unique shape memory effect and pseudoelasticity, as well as good biocompatibility [1]. However, NiTi can be hardly processed by conventional machining techniques due to its poor workability associated with high ductility and work-hardening effect [2]. Besides, the fabrication of NiTi components by traditional processing method is complex and further thermo-mechanical processing is often needed, so the cost of production is high, and the quality is difficult to control. Compared with conventional technologies, additive manufacturing (AM) technology, such as selective laser melting (SLM), has shown its unrivaled capability to fabricate complicated geometrical structures from freeform design. Therefore, AM is very promising in fabricating complex shape NiTi components.

During SLM of NiTi, there are inevitably some imperfections including pores, cracks, microstructure inhomogeneity and impurity pick-up, etc., which may affect product quality and the thermal/mechanical properties of the printed NiTi parts. Study of

imperfections in SLM NiTi is necessary for tailoring product quality and property by defect control, process optimization and post heat treatment. Some work has been conducted with respect to the imperfections in SLM of NiTi alloy. Li et al. [3] found that residual pores and cracks are the main structural defects in Ti-rich NiTi SLM, and heat treatment can improve the homogeneity by dissolute the brittle Ti_2Ni phase. Also, for Ti-rich NiTi SLM, Tan et al. [4] concluded that cracks were aligned normal to the building direction and initiating from the Ti-rich inter-dendritic regions. They also pointed out that the formation of Ti_2Ni and impurity pick-up significantly affect the phase transformation behavior of NiTi. Wang et al. [5] presented that low energy density used in SLM of pre-mixed Ni/Ti powder would induce severe microstructure inhomogeneity, and increasing laser energy density could result in keyhole defects. Haberland et al. [6] got similar results that low energy inputs in Ni-rich NiTi SLM could induce inhomogeneity and concentration difference, leading to very broad and flat transformation peaks. These studies provide initial understanding of formation mechanisms of these imperfections and their effects on microstructure and properties of SLM NiTi alloy.

On the another hand, the era of Industry 4.0 has seen an increasing demand for micro-scale (μ-scale) metallic parts and components in connection with product miniaturization [7]. For NiTi alloy, it is showing a great potential in playing key roles as functional micro-scaled components in micro-actuators, micro-medical devices and implants, micro-mechanical devices, and Micro-Electro-Mechanical Systems (MEMS), etc. In this case, SLM technology needs to be upgraded to meet the increasing demand for NiTi microparts. Regarding to the current scope of SLM in NiTi fabrication, Mahmoudi et al. [8] studied the printability of NiTi by SLM, with cubic NiTi coupons of 10mm×10mm×10mm produced using 100 μm-diameter laser beam. Saedi et al. [9-11] fabricated rectangular and cylindrical NiTi samples by employing Phenix/3D Systems with the beam diameter approximately 80 μm. Xiong [12] achieved superior tensile property and shape memory effect in SLM NiTi with a

50μm-diameter laser beam used. In summary, most of these studies focus on conventional SLM technology, with laser beam diameter ranging from 50~100 μm, which can create large track width. With such large laser beam diameter, the high-precision requirement of manufacturing micro NiTi parts cannot be ensured, which limits the SLM application in micro manufacturing. Scaling down the laser spot size is necessary to increase the fabrication resolution and achieve the micro SLM (μ-SLM).

However, when the laser spot size drops to several micrometers, the underlying mechanism of μ-SLM could be different from that of conventional SLM because of size effect. Concerning the formation and impacts of abovementioned imperfections in μ-SLM of NiTi alloy, the generated knowledge in conventional SLM cannot be applied directly to μ-SLM. Therefore, it is essential to comprehend the mechanisms of imperfections in μ-SLM process and the resultant NiTi microstructures and properties. To the authors' knowledge, μ-SLM of NiTi alloy has never been studied, neither have the imperfections related to μ-SLM NiTi.

In this study, we adopted a self-developed μ-SLM machine equipped with a finer laser beam of 15 μm in diameter to fabricate NiTi parts. The main objective of this study is to analyze and explain the imperfections in NiTi alloy fabricated by μ-SLM, regarding to defects, microstructures and thermal/mechanical behaviors. The underlying mechanisms of various imperfections in processing quality, microstructures and thermal/mechanical behaviors were discussed. The knowledge generated from this work can provide a guideline for defect control, process optimization, as well as post heat treatment methods, and it will better facilitate the development of μ-SLM technology in fabricating functional NiTi products.

2. Material and Experiment

2.1 Material and procedure

Pre-alloyed NiTi powder, produced by gas atomization from $Ni_{55.5}Ti_{44.5}$ (wt. %) ingot, was used to fabricated NiTi parts. The morphology of NiTi powder observed by scanning electron microscopy (SEM), as shown in Fig. 1(a), exhibits a spherical shape, which ensures good flowability during laser melting process. The nominal particle size distribution is 10 ~ 53 μm. As shown by the Energy Dispersive Spectrometer (EDS) result, the Ni and Ti elements are distributed uniformly (Fig. 1(c) and 1(d)), and the total atomic Ni/Ti ratio(including NiTi matrix and the possible secondary phases) is calculated to be less than 1 (Fig. 1(e)).

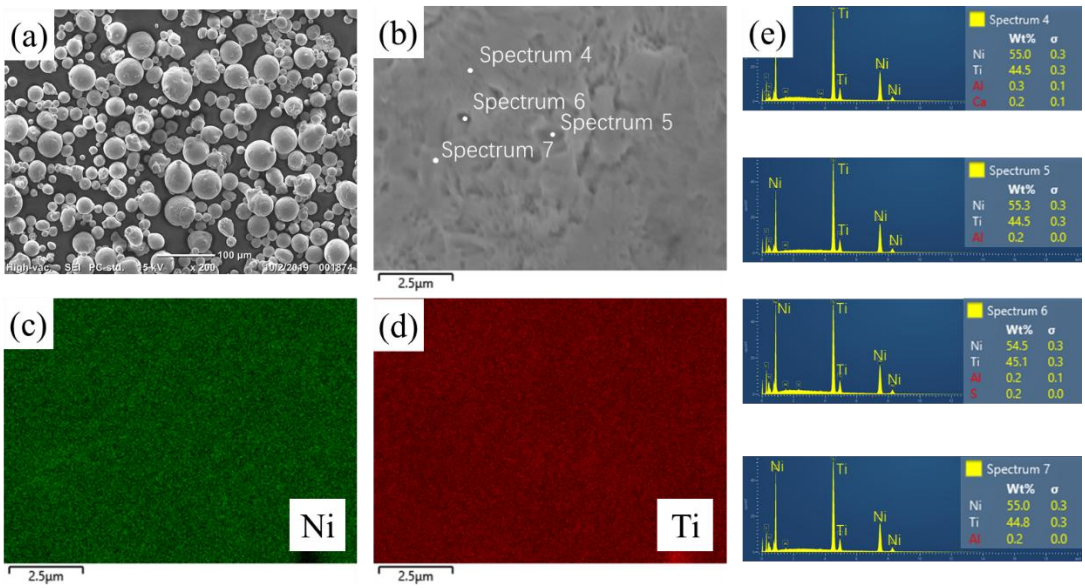

Fig. 1 SEM/EDS characterization of NiTi powder: (a) morphology of powders, (b) cross-section of the powder and locations of the EDS sampling points, (c) Ni element distribution, (d) Ti element distribution and (e) EDS peaks of four points

A self-developed μ-SLM machine in Singapore Institute of Manufacturing Technology (SIMTech), equipped with a continuous 100 W IPG fiber laser (λ=1.07 μm), was employed to fabricate NiTi parts. This μ-SLM equipment has unrivaled advantages over other SLM machines, such as a very small laser spot size of 15 μm and a high precision of 1 μm for building platform. Cylindrical NiTi samples with the diameter of 2.6 mm and height of 3 mm were built with central axis parallel to the building direction under nitrogen gas atmosphere.

The macro and micro defects of the μ-SLM NiTi samples were firstly studied by considering the effects of substrate material, laser-related parameters and laser scanning strategy. Table 1 shows the design of experiments for effect of process parameters on defects. It should be noted the laser power and layer thickness were set as 80 W and 20 μm, respectively. For Set 1 and Set 2, NiTi and Ti substrates were used for comparison to evaluate the effect of substrate material on processing quality. Both substrates were preheating to 80 °C for powder coating and subsequent sample building. Besides, effect of "Scanning speed (V) – Hatch spacing (H)" configuration was studied, with a process window for "H-V" to be determined. In Set 3, the "H-V" configuration was selected according to the process window determined by Set 2. The effect of laser scanning strategy on processing quality was studied, with varying scanning vector rotation angle (hatch angle) of 45/60/90°, as shown in Fig. 2. The corresponding samples are denoted as A45, A60 and A90, respectively.

Then, with the optimal selection of substrate material and process configuration, the microstructure and thermal/mechanical behaviors of as-printed and post heat-treated NiTi samples were compared, and the imperfections in microstructure and thermal/mechanical property were studied. The post heat-treated samples were obtained by either 5.5h annealing treatment at 950°C (HT1 sample), or 10h ageing at 450°C after same annealing treatment (HT2 sample), from as-printed samples. The post heat treatment was conducted in a vacuum furnace with continuous flowing argon atmosphere, and the samples were cooled down by cold flowing argon in the furnace to room temperature.

Table 1 Parametric experiments for effect of process parameters on defects

Process parameter	Scanning speed (V, mm/s)	Hatch spacing (H, μm)	Hatch angle (°)	Substrate material	Remark
Set 1	200/400/600 /800/1000	20/35/50 /65/80	90	Ti	effect of substrate material;

Set 2	200/400/600 /800/1000	20/35/50 /65/80	90	NiTi	effect of H and V; process window for H-V
Set 3	200	35	45/60/90	NiTi	effect of hatch angle

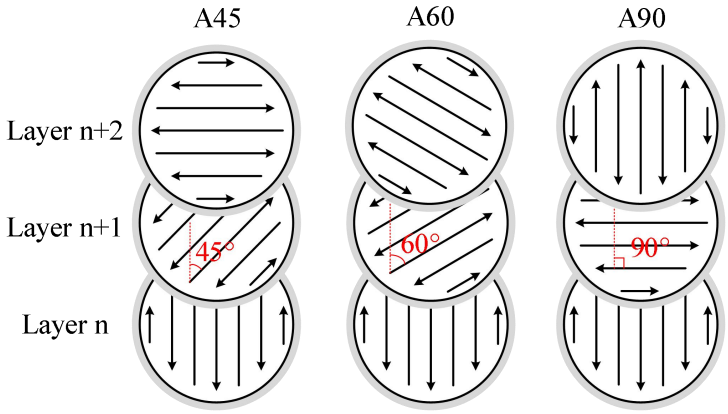

Fig. 2 Scanning strategies with different scan vector rotation angles

2.2 Characterization methods

Optic microscopy (OM) observations were conducted to detect the macro and micro defects of μ-SLM produced NiTi samples, which were etched by a solution composed of 5% HF, 15% HNO_3 and 80% H_2O in volume fraction. The image analysis software ImageJ was used to statistically measure the porosity of the μ-SLM NiTi samples. Each porosity result was averaged from 3 repeated samples and 5 OM images for each data point. Mettler Toledo DSC differential scanning calorimetry (DSC) was used to evaluate the phase transformation temperatures of μ-SLM NiTi under nitrogen atmosphere with heating and cooling rate of 10 °C/min. A high resolution Rigaku SmartLab X-ray diffractometer (HRXRD) was utilized to identify the phases existing in the SLM NiTi samples at room temperature, with 2-Theta angle from 20 ° to 100 °, scanning speed of 5 °/min and step size of 0.01°. SEM observations were conducted on JCM-6000PLUS and VEGA3 TESCAN to characterize the powder morphology, as well as microstructure of as-printed and post heat-treated μ-SLM NiTi samples. EDS was used to capture the chemical composition of specific point or area. ImageJ software was used to measure the grain size and fraction of secondary phase from 8

images for each sample. Vicker hardness was tested on the FM-7E hardness tester with a load of 200g for 15s, and 10 indents on each mechanically polished sample surface were measured to calculate the average value. The compressive mechanical properties of the μ-SLM NiTi samples were evaluated by uniaxial monotonic compressive tests at a rate of 0.2 mm/min on MTS Alliance RT/50 uniaxial testing machine at room temperature. Before testing, the samples were pre-loaded with -20N and lubricating oil was used on the bottom and top surfaces of the samples to reduce the radial friction. For each sample, compressive tests were repeated for three times to ensure the repeatability of mechanical property data.

3. Results and Discussion

3.1 Macro and micro defects in μ-SLM NiTi

In this section, the formation mechanisms of the macro and micro defects, including delamination, cracks, pores, etc., were studied by considering the effects of substrate material, process parameters and scanning strategy.

3.1.1 Effect of substrate material

Fig. 3 shows the NiTi samples that were printed on Ti and NiTi substrates, respectively. About half of the designed samples were automatically unrooted from the Ti building plate during SLM, as shown in Fig. 3(a). The remaining samples were all distorted on the bottom position and delaminated from Ti substrate. The bonding force between NiTi samples and Ti substrate is so weak that the samples can be removed manually. In contrast, most of the cylindrical NiTi samples remained on NiTi substrate with a strong bonding force (Fig. 3(b)), except some built with inappropriate parameter. No delamination was found between NiTi substrate and the remaining samples, which need to be removed by wire cutting, indicating strong bonding force between NiTi samples and the NiTi substrate.

There are several reasons for the low bonding force between the NiTi samples and the

Ti substrate. Firstly, during melting of the first several powder layers, Ti element in the melted Ti substrate will migrate to the molten pool and interact with Ni element. As can be confirmed by SEM/EDS characterization in Fig. 4, a number of brittle intermetallic phases Ti_2Ni were formed near the NiTi/Ti interface, leading to brittleness of the solidified metal. Crack formation is prone to occur under the combination of the brittleness with thermal stresses [13], which is the second important factor. Due to the difference in thermal conductivity and thermal expansion coefficient, 21.9 $W \cdot m^{-1} \cdot K^{-1}$ and 11×10^{-6}/K for pure Ti and 18 $W \cdot m^{-1} \cdot K^{-1}$ and 6.6×10^{-6}/K for NiTi, larger thermal gradient and residual stress can be generated over the combination between NiTi sample and Ti substrate. The high value of residual stress over the boundary between substrate and sample in SLM was experimentally proved by Yadroitsev et al. [14] and numerically simulated by Li et al [15]. According to temperature gradient mechanism (TGM) [16], the plastically compressed upper layer starts shrinkage during cooling and a bending angle towards the laser beam develops, introducing a tensile stress in the building direction. With more layers being deposited, the bending angle increases because of accumulative residual stress, finally causing warping and delamination of NiTi samples from Ti substrate so as to release the residual stress. Last but not least, since Ti and NiTi have different crystal structures, “epitaxial solidification” cannot be ensured, which refers to epitaxial growth of grains in sublayers during solidification [17]. Though the top surface of Ti substrate could be melted during laser scanning of first layer, the grains in Ti layer can hardly grow into the deposited NiTi layer. Therefore, the similarity of material chemical composition and crystal structure between the sample and substrate is very important. Though NiTi is more expensive than Ti, NiTi substrate should be used to ensure effective sample building.

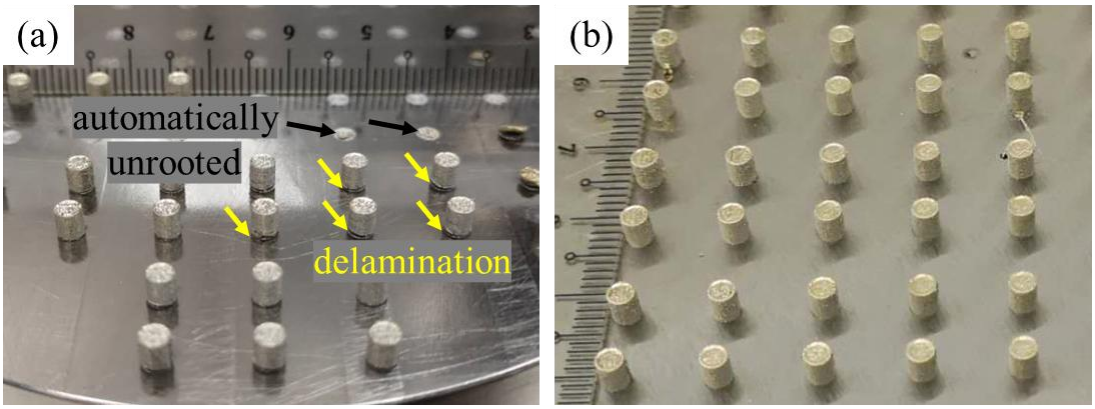

Fig. 3 Samples built on Ti (a) and NiTi (b) substrate

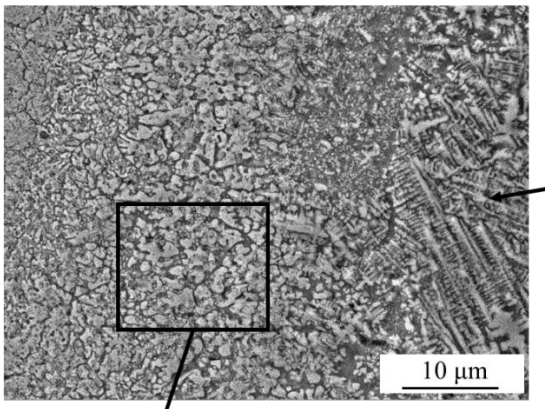

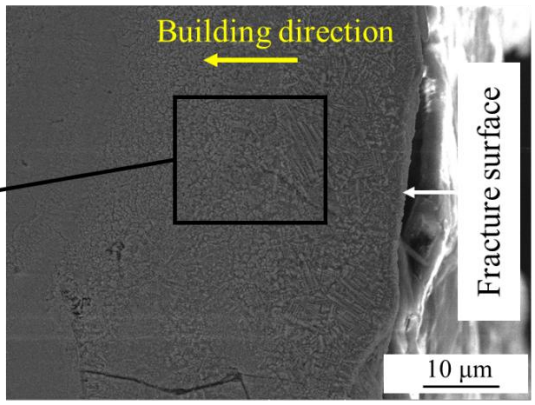

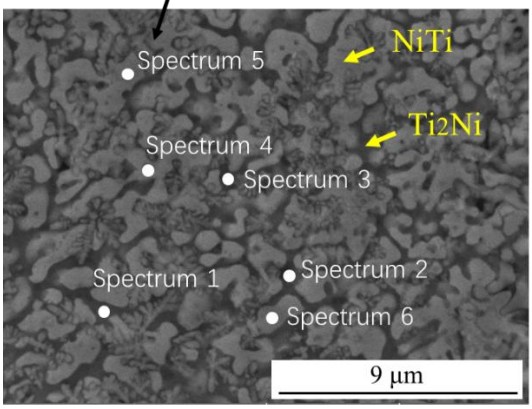

Atomic%	Ti	Ni
Spec 1	64.10	35.90
Spec 2	66.91	33.09
Spec 3	65.16	34.84
Spec 4	56.69	43.41
Spec 5	54.43	45.57
Spec 6	58.38	41.62

Fig. 4 SEM/EDS characterization of bottom area of NiTi sample fractured from Ti substrate

3.1.2 Effect of process parameter

Many studies used laser energy density (Ev) as a criterion to optimize the process parameters [6, 18]. Ev is a combination of various parameters, i.e. Ev=P/(H*V*t), where P is the laser power and t the layer thickness. It is difficult to separate the effect of individual factor. Even with same Ev, different parameter combinations induce

different product quality. Table 2 shows the porosity of samples printed by 21 different “V-H” combinations with corresponding samples denoted from NO. 1 to NO. 21, and corresponding Ev is calculated. NO. 16 sample is printed using the same energy density of 250 J/mm^3 but different parameters as NO. 5 sample. However, the porosity of NO. 16 sample is larger, reaching 5.4%. Besides, some irregular pores and cracks are formed in NO. 16 sample, as shown in Fig. 5(c), which shows the defect morphology of typical μ-SLM NiTi sample. Moreover, Ev only considers three process parameters, ignoring factors like the laser spot size, which is different in traditional SLM and μ-SLM. Therefore, using Ev as an indicator to optimize the process window of μ-SLM can be misleading, while investigation of individual process parameter is rational [8, 19].

A porosity less than 0.43% is achievable with the parameter configurations circled by green lines. The NO. 1 sample severely inflates in shape (Fig. 5(f), NO. 1) due to much longer exposure time (point distance divided by scanning speed) and resultant over melting, which could induce high oxygen pick-up from chamber atmosphere. For NO. 2-5 samples, there isn’t an obvious trend for the effect of H on porosity, as proved by OM images of NO.2 and NO. 5 in Fig. 5(a, b). However, the porosity of the printed samples is much sensitive to V. Taking H of 20 μm as an example, with increasing V, the exposure time and the molten pool depth decrease, as a consequence, the samples either incurred higher porosity or failed because of delamination (Fig. 5(f), NO. 19). Some spherical pores of about 3 μm in diameter can be found for NO. 2 and NO. 5 samples shown in Fig. 5(a, b). These small spherical pores are formed by trapped gas during SLM, possibly originating from the gas present between powder particles, high laser energy induced Ni evaporation and unstable molten pool [20, 21]. Due to high cooling rate, the solidification process impedes the movement of gas bubbles from molten pool to surface area, and finally they remain in the solidified molten pool. Unfortunately, it is very difficult to completely avoid these randomly distributed spherical pores due to nature of μ-SLM process.

With increasing V or H, the fraction of un-melted regions increases, and samples tend towards failure (Fig. 5(c, d and e)). Un-melted regions with the diameter around 100 μm are formed due to insufficient melting caused by shorter exposure time or lack of overlap between adjacent laser tracks or deposited layers. In addition, the possible oxide film forms during SLM may cause poor wettability and block molten metal flow, further induces incomplete fusion defects [22]. As the un-melted regions further propagate due to poor fluid flowability in these regions, weak interlayer bonding will develop to macroscope delamination and failure of SLM part. Thus, sufficient exposure time and appropriate overlap should be ensured to create enough molten pool penetration depth and eliminate the un-melted regions and weak bonding phenomenon.

Fast cooling rate of $10^{3\sim8}$ K/s in SLM can lead to high temperature gradient and high residual thermal stress, causing crack initiation and propagation [23, 24]. Macro and micro cracks are observed in NO. 16, NO. 17 and NO. 20 samples and other failed samples (Fig. 5(f), NO. 15 and 21), resulting from cold cracking. The macro cracks mainly initiate at the edge of the sample, i.e. the lateral, top and bottom surfaces, and propagate towards inside. Similar macro cracks located at the edge of full-density SLM NiTi samples were observed by Li et al [3]. Though the termination of macro cracks relieves the majority of the residual stress, there may be some positions, like grain boundaries and phase interfaces, having problem of stress concentration. In this case, once the internal concentrated stress is higher than yield strength, micro cracks will appear at stress-concentrated areas.

Many studies found that cracks are prone to form with increasing exposure time or decreasing overlap ratio, which causes larger thermal gradient and high residual thermal stress [23, 25]. However, in this study, micro and macro cracks are mainly found in high-porosity and insufficiently melted samples. This is probably because

insufficient melting induces weak bonding force between layers, which cannot overwhelm the high residual stress. Besides, the larger un-melted regions provide convenience for crack propagation to release the residual thermal stress. Also, the high stress concentration in these regions may cause crack initiation [26]. Thus, more cracks were observed in these samples, which even fracture the SLM parts.

Based on the above results, a relatively rough process window was determined as shown in Fig. 6. Region I and III cannot ensure appropriate product quality due to over melting and insufficient melting, respectively. The narrow process window (region II) indicates that the quality of μ-SLM NiTi is sensitive to the process parameters. More parameter configurations need to be designed and conducted to define clear boundaries between the three regions.

Table 2 Parameter configuration and porosity examination

NO.	V (mm/s)	H (μm)	E_v (J/mm^3)	Quality
1	200	20	1000	over melting
2	200	35	571.42	porosity: 0.12%
3	200	50	400.00	porosity: 0.37%
4	200	65	307.69	porosity: 0.27%
5	200	80	250.00	porosity: 0.27%
6	400	20	500.00	porosity: 0.33%
7	400	35	285.70	porosity: 0.15%
8	400	50	200.00	failed
9	400	65	153.84	failed
10	400	80	125.00	failed
11	600	20	333.33	porosity: 0.43%
12	600	35	190.47	failed
13	600	50	133.33	failed
14	600	65	102.56	failed
15	600	80	83.33	failed
16	800	20	250.00	porosity: 5.4%
17	800	35	142.80	failed
18	800	50	100.00	failed
19	1000	20	200.00	failed

20	1000	35	114.28	failed
21	1000	50	80.00	failed

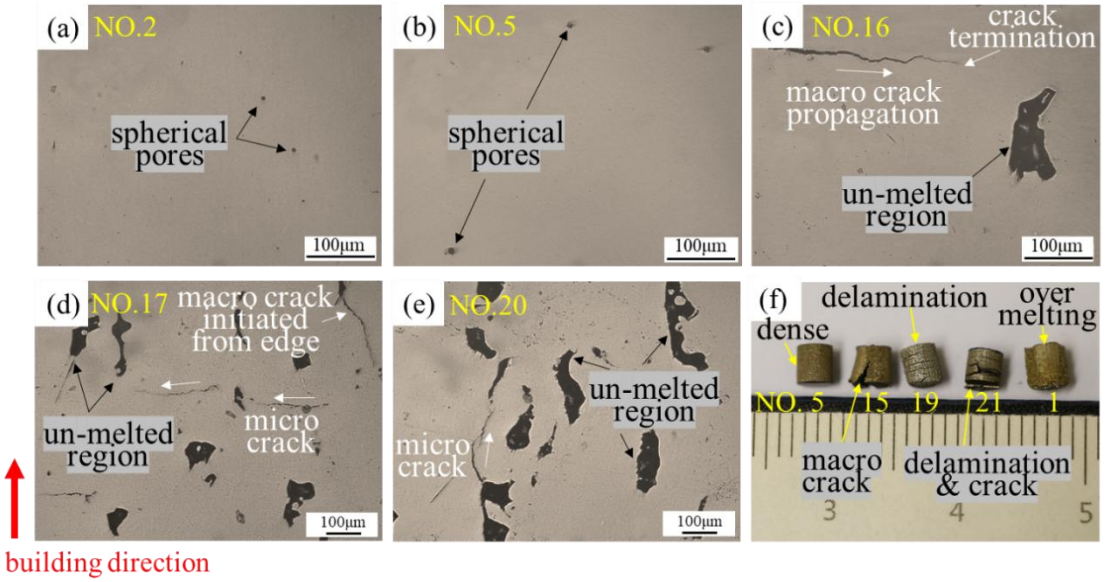

Fig. 5 Macro and micro defects of samples (vertical section)

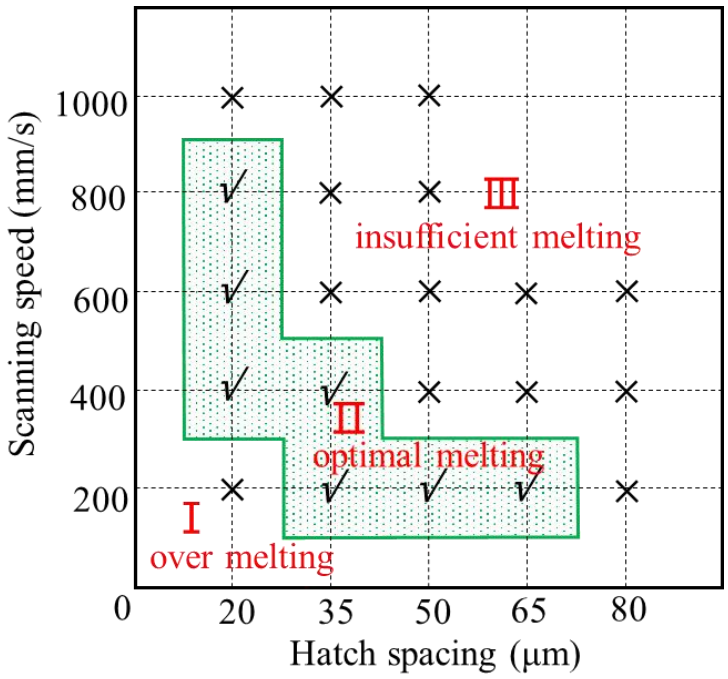

Fig. 6 Process window for Hatch spacing-Scanning speed

3.1.3 Effect of scanning strategy

The A45, A60 and A90 samples were printed using one of the optimal "V-H"

configurations in process window, i.e. 35 μm of H and 200 mm/s of V, with other parameters unchanged. Fig. 7(a), (b) and (c) are cross-section OM images of A45, A60 and A90, showing morphology of scanning pattern and pore distribution. We can recognize the scanning tracks from the highlighted angle of 45 °, 60 ° and 90° between two tracks in adjacent deposited layers. Different tracks correspond to different scanning vectors. In addition, the herringbone patterns composed of "///" and "\\\" shaped grains were identified in Fig. 7(a). Similar grain structure was observed in the work by Thijs et al. [27, 28] and Bormann et al [19]. This mirrored grain pattern is caused by the inverse adjacent laser scanning direction, which alternates the heat transfer direction and forms a mirrored heat flux along transverse direction [28]. As grains grow opposite to the heat flux, such herringbone pattern is then formed. Irregular scanning tracks were also observed in A60 and A90 samples, reflecting the unstable molten pool, which is responsible for defect formation, such as balling effect and cracking.

Gas pores are observed in all the three samples. The porosity of μ-SLM NiTi samples under the three scanning strategies are statistically detected, as shown in Fig. 7(d). The average porosity for A45, A60, and A90 samples is small, only 0.086%±0.0253%, 0.098%±0.0256% and 0.12%±0.0294%, respectively. Considering the large randomness of gas pore formation and distribution, the variation of the low porosity associated with the effect of scanning strategy can be neglected. Fig. 7(d) also illustrates the "availability" and hardness of the as-printed samples under different scanning strategies. The "availability" of SLM produced NiTi samples herein refers to the percent of crack-free and low-porosity samples printed by same process parameters, and equals to 100%, 100% and 75% for A45, A60 and A90 sample, respectively. 25% of A90 samples failed because of crack formation. The hardness was measured to be 395.4±7.2HV, 401.4±5.0HV and 407.9±14.26HV for the three scanning strategies, respectively, showing an increasing trend. The lower availability and higher hardness of A90 samples can be attributed to the residual stress affected by

scanning strategy. Liu et al. [29] and Simson et al. [30] revealed that the residual stress is larger along scanning direction than along building direction due to larger thermal gradient, then the track mainly shrinks along the scanning direction. When rotating the laser scanning vector layer by layer, the heat flux direction and thermal gradient will be changed. Comparing A45, A60 and A90 scanning strategies, a more uniform temperature field can be expected by A45, since the scanning vectors under A45 change more frequently with less repeated scanning vector feature. Thus, by rotating the scanning vectors more uniformly, A45 can induce an isotropic stress field in the component [31]. While A90 strategy causes significant directional residual stress, which promotes the crack formation, and the concentrated residual stress also causes higher hardness. As discussed above, A45 and A60 scanning strategies are more preferable than A90 because of reduced risk of crack by residual stress.

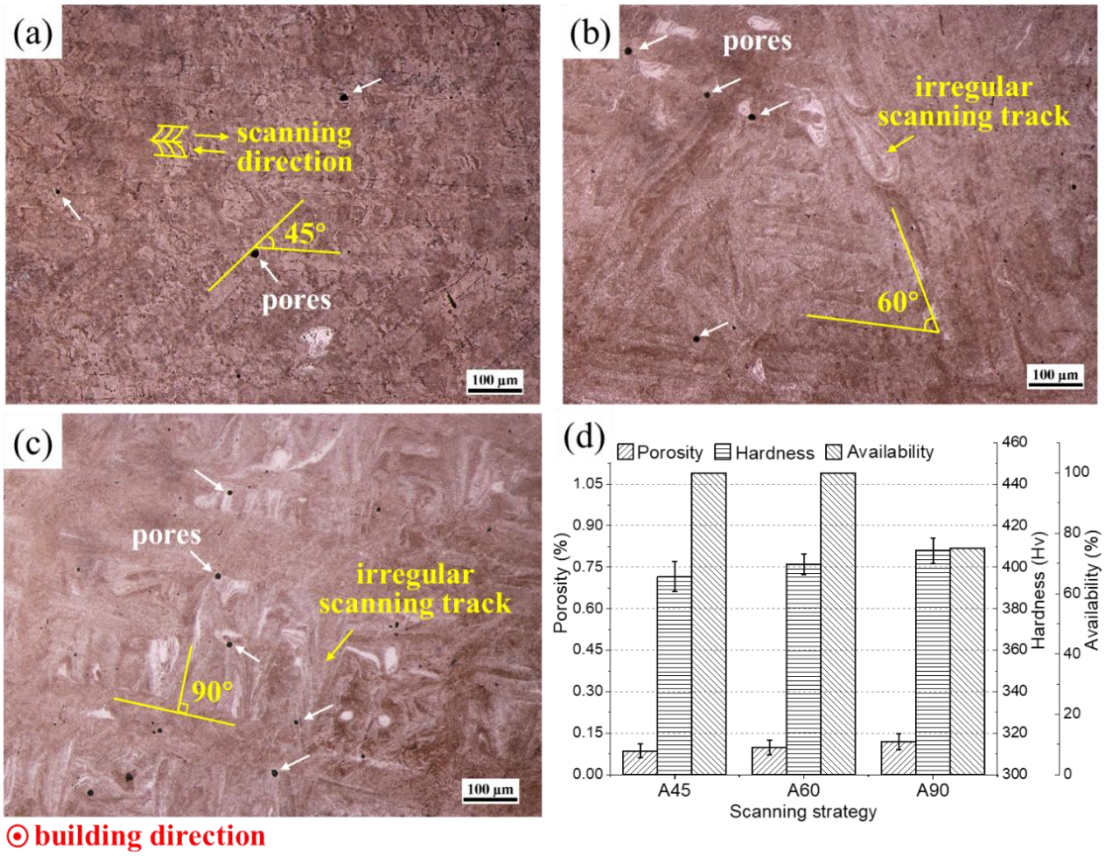

Fig. 7 OM images of μ-SLM NiTi under different scanning strategies: (a) A45, (b) A60, (c) A90; and (d) histogram showing effect of scanning strategy on porosity,

hardness and availability of μ-SLM NiTi

3.2 Microstructure and thermal/mechanical behaviors

In this section, the microstructure and thermal/mechanical behaviors of NiTi powder, as-printed NiTi and post heat-treated μ-SLM NiTi were analyzed.

3.2.1 Analysis of microstructure

Fig. 8 shows XRD profiles of NiTi powder, as-printed NiTi and post heat-treated μ-SLM NiTi. The matrix phase of all the samples is austenitic NiTi with B2 structure, indicating the matrix is Ni-rich. For XRD pattern of NiTi powder, the peak of $Ti_2Ni/Ti_4Ni_2O_x$, marked by "▲", are detected. However, Ti_2Ni cannot be easily found in SEM characterization (Fig. 1) due to the much smaller volume fraction of Ti_2Ni compared with matrix phase. The co-existence of Ni-rich matrix and Ti_2Ni in NiTi powder corresponds to the total atomic Ni/Ti ratio less than 1, as confirmed by the EDS result (Fig. 1e). The volume fraction of $Ti_2Ni/Ti_4Ni_2O_x$ is much smaller compared with matrix phase. The formation of the Ti_2Ni particles may due to the Ti_2Ni precipitation during powder preparation, since the near-equiatomic NiTi may also contain some Ti_2Ni phases. Besides, the Ti_2Ni particles may also form due to oxidation during powder preparation, i.e. the formation of $Ti_4Ni_2O_x$ particles. All the O elements in the NiTi are believed to form the impurity phase $Ti_4Ni_2O_x$ [32], which has nearly the same crystal structure as Ti_2Ni. The $Ti_2Ni/Ti_4Ni_2O_x$ peak disappears in the XRD pattern of as-printed NiTi, mainly because the fast cooling rate of SLM impedes the formation of Ti_2Ni precipitates, and the peak for small number of $Ti_4Ni_2O_x$ cannot be visualized. In addition, another impurity phase, $TiC_{1-x}N_x$, is generated in the as-printed NiTi due to the interaction between molten pool and chamber atmosphere, and it was also detected by other researchers [32, 33]. HT1 and HT2 samples have similar XRD patterns, where Ti_2Ni reappears during both heat treatments. Similarly, apart from Ti_2Ni precipitation, the formation of Ti_2Ni particles could be partially attributed to oxidation during heat treatment, i.e. formation of

$Ti_4Ni_2O_x$. The impurity phase $TiC_{1-x}N_x$ is difficult to be dissolved, always existing in the printed parts. An important precipitate, Ni_4Ti_3, is produced after heat treatment, which can improve the shape memory property and is believed to form only at the Ni content above 50.6 at.% under a temperature below 600°C [34]. Since the precipitation of Ti_2Ni could produce Ni-rich NiTi matrix, Ni_4Ti_3 precipitation during heat treatment process is enabled. Besides, the HT1 and HT2 samples were cooled by cold flowing argon in the furnace to room temperature with the cooling rate of 50 ℃/min, which is much slower than water quenching. Thus, the cooling period may allow the Ni_4Ti_3 precipitation in HT1 sample, while the long-time aging at 450 ℃ for HT2 could bring more Ni_4Ti_3 precipitates. The weak XRD peaks related to NiTi (B19') martensite phase were also detected in HT1 and HT2 samples, although some of the peaks overlap with those of Ti_2Ni phase. The appearing of B19' phase is mainly due to localized variation of Ni/Ti ratio after heat treatment. For instance, since Ni_4Ti_3 phase forms at the expense of Ni, the local matrix phase may be Ti-rich in the vicinity of Ni_4Ti_3 phase, leading to the appearing of B19' phase at room temperature.

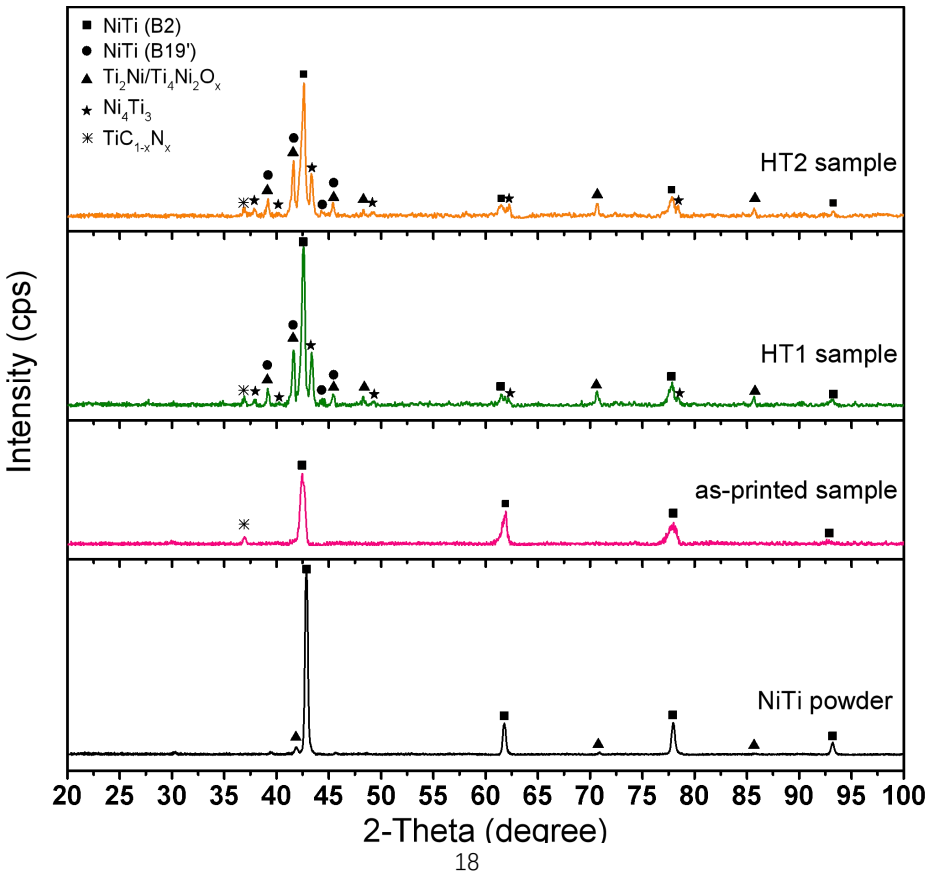

Fig. 8 XRD profiles of NiTi powder, as-printed and heat-treated μ-SLM NiTi samples

Fig. 9 shows the SEM micrographs of as-printed, HT1 and HT2 μ-SLM NiTi samples. The grain boundaries in as-printed NiTi sample are invisible (Fig. 9(a, b)), while they can be distinguished in HT1 and HT2 samples by the contrast difference between grain boundary precipitates (Ti_2Ni, dark) and parent phase (NiTi, gray), as shown in Fig. 9(c, d, e, f). The average grain size in the cross-section was measured to be 4.0±0.3 μm and 4.9±0.5 μm in HT1 and HT2 samples, respectively, smaller than that in some other literatures [9, 35]. The grain refinement benefits from finer scanning track and fast cooling rate in μ-SLM. In addition, the columnar grain forms as a result of epitaxial solidification, which causes the growth of grains in sublayers along building direction against heat flux [17].

The average fraction of Ti_2Ni phases in HT1 and HT2 sample is measured to be 16.21% and 20.59%, respectively, suggesting that the aging temperature of 450 °C facilitates the nucleation or growth of Ti_2Ni phases. Same microstructure was observed by Tan et al [4]. In fact, Ti_2Ni phase could significantly affect the property of μ-SLM NiTi parts. On the one hand, the brittleness of this phase can weaken the mechanical properties by initiating crack during service of μ-SLM NiTi parts. On the other hand, the Ti-rich Ti_2Ni phase precipitates by depleting Ti element in NiTi matrix. The Ni/Ti ratio is then changed, which influence the phase transformation behavior and functional properties.

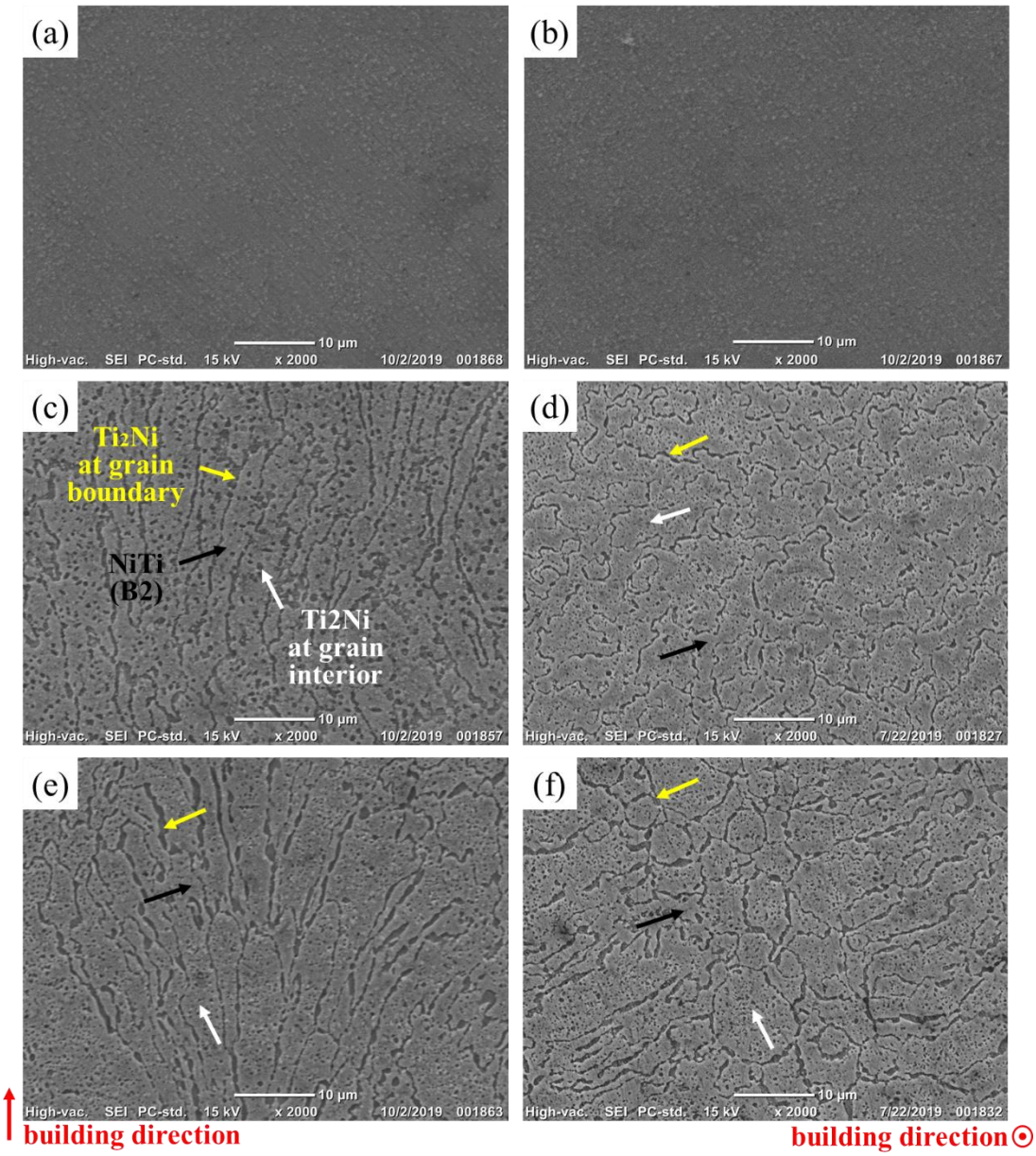

Fig. 9 SEM micrographs showing microstructures of: (a, b) as printed sample, (c, d) HT1 sample, (e, f) HT2 sample; (a, c, e) vertical section, (b, d, f) cross section

3.2.2 Analysis of thermal-induced phase transformation behavior

Fig. 10 shows the DSC curves of NiTi powder, as-printed and heat-treated NiTi parts. The phase transformation temperatures (TTs) for NiTi powder can be identified but the transformation peak of NiTi powder is very broad, as shown in Fig. 10(a). Austenite transformation end temperature A_f is 15.5 °C, below the room temperature, which explains why B2 NiTi was identified by XRD tests at room temperature. While

for as-printed and HT1 sample (Fig. 10(b, c)), no transformation peak was detected, with TTs decreased and thermal-induced martensite transformation suppressed. Such decrease of TTs is mainly attributed to several factors as follows. Firstly, the precipitation of Ti_2Ni consumes Ti element from NiTi matrix and induce Ni-rich matrix. The TTs decrease with increasing Ni content in NiTi matrix [36]. Secondly, the impurity pick-up of O, C, and N element can induce un-dissolvable second phases ($TiC_{1-x}N_x$ and $Ti_4Ni_2O_x$) and depress martensite transformation. This is related to the fact that the impurity phases form at expense of Ti consumption in NiTi matrix. The relationship between the impurity content (O, C) and M_s can be expressed using empirical equations [4, 37]:

$$M_s = 78°C - 92.63\frac{°C}{wt.\%}x_o$$

$$M_s = 7.5°C - 73.3\frac{°C}{at.\%}x_c$$

where x_o and x_c represent the oxygen and carbon content. According to the above relationship, M_s decreases by about 92.63°C/wt. % and 73.3°C/at. % with increasing oxygen and carbon content, respectively. Therefore, the decrease of TTs mainly comes from variation of matrix Ni/Ti ratio due to formation of Ti_2Ni, $TiC_{1-x}N_x$ and $Ti_4Ni_2O_x$ phases, which form during powder preparation, SLM and post heat treatment.

The wide TTs range and the hardly detectable transformation peak are attributed to microstructure inhomogeneity[6, 38], which leads to gradual and suppressed phase transformation behavior. On the one hand, the sever impurity pick-up during powder preparation, SLM process and the high temperature heat treatment may be the main reason for the significant suppression of the transformation, since the secondary phases including $TiC_{1-x}N_x$ and $Ti_4Ni_2O_x$ result in inhomogeneous microstructure and localized stress field. One the other hand, chemical segregation induced by SLM, i.e., a small concentration of Ni solute might be pushed towards the edges of the laser tracks with the Marangoni flows during laser melting [39], causing inhomogeneous composition distribution.

As shown in Fig. 10(d), a small transformation peak was detected in HT2 sample, which represents R phase transformation. It is a thermo-elastic transformation between the B2 austenite phase and a rhombohedral R-phase, which occurs prior to the formation of B19' martensite phase during cooling, thanks to the presence of crystallographic defects (e.g., dislocations or Ni_4Ti_3 precipitates) [36]. In HT2 sample, the 10h ageing process at 450°C introduces many Ni_4Ti_3 precipitates. As a result, the R phase transformation occurs during cooling from a high temperature (i.e. 80 °C in this DSC test), while the B19' martensite transformation is still suppressed. As measured, the room temperature (25 °C) is lower than the R phase transformation start temperature (R_s=46 °C), but higher than the R phase transformation end temperature (R_f=13.5 °C). In this case, R phase is believed to exist in the as-printed NiTi parts at room temperature. However, the R phase was not detected in room-temperature XRD test. This indicates that B2 austenite phases were partially transformed to R phases, and only a small number of R phases were formed, which cannot be detected in XRD tests. It should be noted that for HT1 sample, the small number of Ni_4Ti_3 phases can hardly facilitate R phase transformation. Thus, there is no R phase transformation peak detected in the DSC curve of HT1 sample.

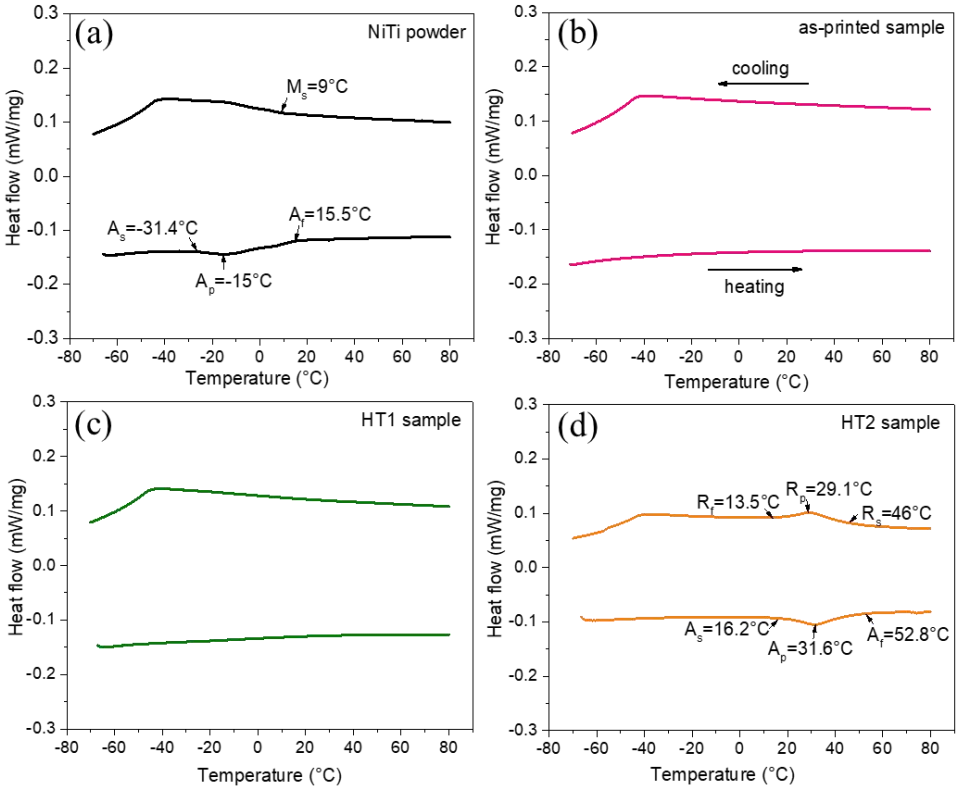

Fig. 10 DSC curves of NiTi powder, as-printed and heat-treated μ-SLM NiTi samples

3.2.3 Analysis of compressive deformation behavior

Fig. 11 illustrates the room-temperature compressive deformation behavior of as-printed and heat-treated μ-SLM NiTi samples. The as-printed NiTi sample shows higher compressive strength and fracture strain, averagely reaching 2796.3 MPa and 28.4%, respectively. The HT1 and HT2 NiTi samples present similar compressive strength and fracture strain, 2497.2 MPa and 12.6% for HT1, and 2604.4 MPa and 12.1% for HT2, both lower than those of as-printed NiTi sample. The underlying factor can be attributed to Ti_2Ni phase. Though Ti_2Ni can induce precipitate strengthening effect, it is so brittle as to make the material sensitive to stress concentration and crack propagation along Ti_2Ni at the grain boundaries and decrease both the compressive strength and ductility. Therefore, the heat-treated samples, which contain more brittle Ti_2Ni, shows worse compressive property than the as-printed, and neither obvious transformation strain nor plastic strain occurs. HT2 sample has slightly higher strength than HT1 sample because of the additional

strengthening effect of Ni_4Ti_3 precipitates.

For as-printed SLM NiTi samples, the compressive stress-strain behavior shows three distinguishable stages. Stage I indicates elastic deformation of austenitic B2 phase. The presence of Ti-rich secondary phases depresses martensite transformation and decreases M_s dramatically, so the critical stress for stress-induced martensite transformation (σ_{SIM}) becomes much higher, approximately 1200 MPa (left enlarged inset), as compared with other works [38, 40-42], where σ_{SIM} ranges from 200 ~ 900MPa. This can be explained according to Clausius–Clapeyron-type relationship [36]:

$$\frac{d\sigma}{dT} = -\frac{\Delta S}{\varepsilon} = -\frac{\Delta H^*}{\varepsilon T}$$

where σ is a uniaxial applied stress, ε a transformation strain, ΔS the entropy of transformation per unit volume, and ΔH^* the enthalpy of transformation per unit volume. This equation gives the dependence of σ_{SIM} on temperature. For forward transformation from austenite to martensite, ΔS and ΔH^* are negative, and the slope of $d\sigma/dT$ is positive. With increasing temperature in $T>M_s$ region, the critical stress for introducing martensite transformation will increase. At constant testing temperature, σ_{SIM} increases with decreasing M_s.

In stage II, plateau stress-strain behavior is indistinguishable due to the inhomogeneous and localized stress-induced martensite transformation (SIMT). Several studies have confirmed the inhomogeneous SIMT strain by digital image correlation (DIC) analysis [43, 44]. This phenomenon is probably related to the presence of Ti-rich impurities and inhomogeneous chemical composition distribution in μ-SLM NiTi. With increasing applied stress, a growing number of austenite phases in a wide range gradually transform to martensite, simultaneously accompanied by martensitic elastic deformation. Thus, stage II probably includes SIMT and elastic deformation of martensite. With further loading, plastic deformation of martensite occurs in stage III. The wave-like curve indicates a Portevin–Le Chatelier (PLC)

effect, which is commonly seen in deformation process of aluminum alloys [45]. The stress fluctuation is mainly caused by dislocation movement. The solute atoms could impede dislocation slip, leading to pining effect and stress increase. When the applied stress is high enough to overcome the energy barrier, dislocations can pass over the solute atoms, and the stress drops. This zigzag fluctuation repeats until sample fracture.

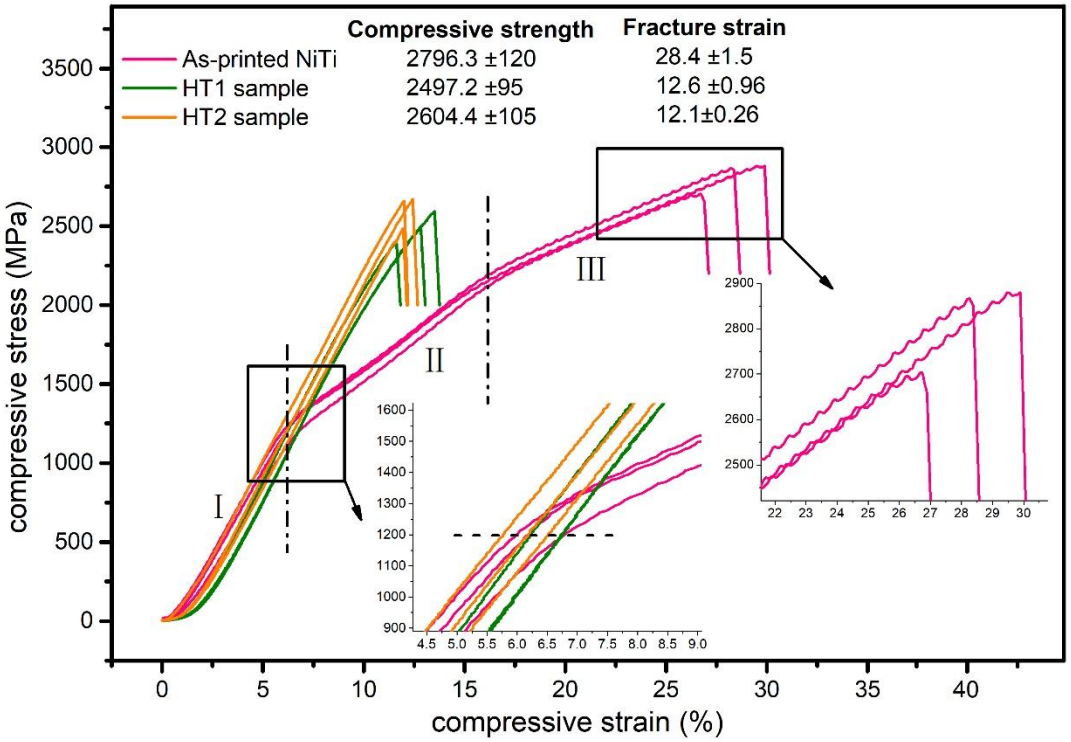

Fig. 11 Engineering compressive stress-strain curves of as-printed and heat-treated μ-SLM NiTi samples

4 Conclusions

In this study, NiTi shape memory alloy parts were fabricated by micro selective laser melting (μ-SLM). The imperfections including defects, microstructure and thermal/mechanical behaviors of μ-SLM NiTi were analyzed, and the underlying mechanisms were discussed. The main findings can be summarized as follows:

(1) Compared with NiTi substrate, Ti substrate cannot ensure effective sample building because of sample delamination from substrate. The similarity of

material chemical composition and crystal structure between the sample and substrate should be guaranteed.

(2) The formation mechanisms of μ-SLM induced structure defects including gas pores, un-melted regions and cracks were analyzed. A process window for "Scanning speed – Hatch spacing" was determined to produce low-porosity and crack-free NiTi samples.

(3) A90 scanning strategy induces lower availability and higher hardness of μ-SLM NiTi than A45 and A60 scanning strategy do. A45 and A60 scanning strategies are more preferable because of lower residual stress and reduced risk of crack.

(4) The martensite transformation was depressed, and transformation peak was hardly detected in thermal behavior of as-printed and post heat-treated μ-SLM NiTi, resulting from microstructure inhomogeneity and Ti-rich impurity phases $TiC_{1-x}N_x/Ti_4Ni_2O_x$ and precipitate Ti_2Ni.

(5) The as-printed NiTi shows higher compressive strength and fracture strain, averagely reaching 2796.3 MPa and 28.4%, respectively, but the plateau stress-strain stage by stress-induced martensite transformation is indistinguishable. The brittle Ti_2Ni phase introduced by post heat treatment leads to inhomogeneous microstructure and lower ductility.

Acknowledgments

FU Jin would like to acknowledge the financial support from The Hong Kong Polytechnic University (NO. 1-ZVMR), and National Natural Science Foundation of China (NO. 51775441). HU Zhiheng would like to acknowledge the financial support from the Agency for Science, Technology and Research (A*STAR) - Science and Engineering Research Council of Singapore (SERC Grant no. 142 68 00088). SONG Xu would like to acknowledge the financial support from the Chinese University of Hong Kong (CUHK) – Start-up Fund (No. 153).

References

[1] N. Morgan, Medical shape memory alloy applications—the market and its products, Mater. Sci. Eng., A 378 (2004) 16-23.

[2] J.P. Oliveira, R.M. Miranda, F.M. Braz Fernandes, Welding and Joining of NiTi Shape Memory Alloys: A Review, Prog. Mater. Sci 88 (2017) 412-466.

[3] S. Li, H. Hassanin, M.M. Attallah, N.J.E. Adkins, K. Essa, The development of TiNi-based negative Poisson's ratio structure using selective laser melting, Acta Materialia 105 (2016) 75-83.

[4] C. Tan, S. Li, K. Essa, P. Jamshidi, K. Zhou, W. Ma, M.M. Attallah, Laser Powder Bed Fusion of Ti-rich TiNi lattice structures: Process optimisation, geometrical integrity, and phase transformations, Int. J. Mach. Tool Manu. 141 (2019) 19-29.

[5] C. Wang, X.P. Tan, Z. Du, S. Chandra, Z. Sun, C.W.J. Lim, S.B. Tor, C.S. Lim, C.H. Wong, Additive manufacturing of NiTi shape memory alloys using pre-mixed powders, J. Mater. Process. Technol. 271 (2019) 152-161.

[6] C. Haberland, M. Elahinia, J.M. Walker, H. Meier, J. Frenzel, On the development of high quality NiTi shape memory and pseudoelastic parts by additive manufacturing, Smart. Mater. Struct. 23 (2014).

[7] M. Fu, J. Wang, A. Korsunsky, A review of geometrical and microstructural size effects in micro-scale deformation processing of metallic alloy components, Int. J. Mach. Tool Manu. 109 (2016) 94-125.

[8] M. Mahmoudi, G. Tapia, B. Franco, J. Ma, R. Arroyave, I. Karaman, A. Elwany, On the printability and transformation behavior of nickel-titanium shape memory alloys fabricated using laser powder-bed fusion additive manufacturing, J. Manuf. Process. 35 (2018) 672-680.

[9] S. Saedi, N. Shayesteh Moghaddam, A. Amerinatanzi, M. Elahinia, H.E. Karaca, On the effects of selective laser melting process parameters on microstructure and thermomechanical response of Ni-rich NiTi, Acta Materialia 144 (2018) 552-560.

[10] S. Saedi, A.S. Turabi, M.T. Andani, N.S. Moghaddam, M. Elahinia, H.E. Karaca, Texture, aging, and superelasticity of selective laser melting fabricated Ni-rich NiTi

alloys, Mater. Sci. Eng., A 686 (2017) 1-10.

[11] S. Saedi, A.S. Turabi, M. Taheri Andani, C. Haberland, H. Karaca, M. Elahinia, The influence of heat treatment on the thermomechanical response of Ni-rich NiTi alloys manufactured by selective laser melting, J. Alloys Compd. 677 (2016) 204-210.

[12] Z.W. Xiong, Z.H. Li, Z. Sun, S.J. Hao, Y. Yang, M. Li, C.H. Song, P. Qiu, L.S. Cui, Selective laser melting of NiTi alloy with superior tensile property and shape memory effect, J. Mater. Sci. Technol. 35 (2019) 2238-2242.

[13] A.S. Zoeram, S.A. Mousavi, Laser welding of Ti–6Al–4V to Nitinol, Mater. Des. 61 (2014) 185-190.

[14] I. Yadroitsev, I. Yadroitsava, Evaluation of residual stress in stainless steel 316L and Ti6Al4V samples produced by selective laser melting, Virtual and Physical Prototyping 10 (2015) 67-76.

[15] C. Li, J. Liu, X. Fang, Y. Guo, Efficient predictive model of part distortion and residual stress in selective laser melting, Addit. Manuf. 17 (2017) 157-168.

[16] P. Mercelis, J.-P. Kruth, Residual stresses in selective laser sintering and selective laser melting, Rapid Prototyping J. 12 (2006) 254-265.

[17] M. Elahinia, N. Shayesteh Moghaddam, M. Taheri Andani, A. Amerinatanzi, B.A. Bimber, R.F. Hamilton, Fabrication of NiTi through additive manufacturing: A review, Prog. Mater. Sci 83 (2016) 630-663.

[18] G. Casalino, S. Campanelli, N. Contuzzi, A. Ludovico, Experimental investigation and statistical optimisation of the selective laser melting process of a maraging steel, Opt. Laser Technol. 65 (2015) 151-158.

[19] T. Bormann, B. Müller, M. Schinhammer, A. Kessler, P. Thalmann, M. de Wild, Microstructure of selective laser melted nickel–titanium, Mater. Charact. 94 (2014) 189-202.

[20] B. Zhang, Y. Li, Q. Bai, Defect formation mechanisms in selective laser melting: a review, Chin. J. Mech. Eng. 30 (2017) 515-527.

[21] Z. Hu, H. Zhu, H. Zhang, X. Zeng, Experimental investigation on selective laser melting of 17-4PH stainless steel, Opt. Laser Technol. 87 (2017) 17-25.

[22] N. Read, W. Wang, K. Essa, M.M. Attallah, Selective laser melting of AlSi10Mg alloy: Process optimisation and mechanical properties development, Mater. Des. 65 (2015) 417-424.

[23] D.D. Gu, Y.C. Hagedorn, W. Meiners, G.B. Meng, R.J.S. Batista, K. Wissenbach, R. Poprawe, Densification behavior, microstructure evolution, and wear performance of selective laser melting processed commercially pure titanium, Acta Materialia 60 (2012) 3849-3860.

[24] R.F. Hamilton, T.A. Palmer, B.A. Bimber, Spatial characterization of the thermal-induced phase transformation throughout as-deposited additive manufactured NiTi bulk builds, Script. Mater. 101 (2015) 56-59.

[25] L.N. Carter, X. Wang, N. Read, R. Khan, M. Aristizabal, K. Essa, M.M. Attallah, Process optimisation of selective laser melting using energy density model for nickel based superalloys, Mater. Sci. Technol. 32 (2016) 657-661.

[26] H. Shipley, D. McDonnell, M. Culleton, R. Coull, R. Lupoi, G. O'Donnell, D. Trimble, Optimisation of process parameters to address fundamental challenges during selective laser melting of Ti-6Al-4V: A review, Int. J. Mach. Tool Manu. 128 (2018) 1-20.

[27] L. Thijs, F. Verhaeghe, T. Craeghs, J. Van Humbeeck, J.-P. Kruth, A study of the microstructural evolution during selective laser melting of Ti–6Al–4V, Acta Materialia 58 (2010) 3303-3312.

[28] L. Thijs, M.L.M. Sistiaga, R. Wauthle, Q.G. Xie, J.P. Kruth, J. Van Humbeeck, Strong morphological and crystallographic texture and resulting yield strength anisotropy in selective laser melted tantalum, Acta Materialia 61 (2013) 4657-4668.

[29] Y. Liu, Y. Yang, D. Wang, A study on the residual stress during selective laser melting (SLM) of metallic powder, Int. J. Adv. Manuf. Technol. 87 (2016) 647-656.

[30] T. Simson, A. Emmel, A. Dwars, J. Böhm, Residual stress measurements on AISI 316L samples manufactured by selective laser melting, Addit. Manuf. 17 (2017) 183-189.

[31] L. Parry, I. Ashcroft, R.D. Wildman, Understanding the effect of laser scan

strategy on residual stress in selective laser melting through thermo-mechanical simulation, Addit. Manuf. 12 (2016) 1-15.

[32] P. Olier, F. Barcelo, J.L. Bechade, J.C. Brachet, E. Lefevre, G. Guenin, Effects of Impurities Content (Oxygen, Carbon, Nitrogen) on Microstructure and Phase Transformation Temperatures of Near Equiatomic TiNi Shape Memory Alloys, Le Journal de Physique IV 07 (1997) C5-143-C5-148.

[33] B. Bertheville, J.E. Bidaux, Enhanced powder sintering of near-equiatomic NiTi shape-memory alloys using Ca reductant vapor, J. Alloys Compd. 387 (2005) 211-216.

[34] K. Otsuka, C. Wayman, Mechanism of shape memory effect and superelasticity, Shape memory materials(1998) 27-48.

[35] T. Bormann, R. Schumacher, B. Muller, M. Mertmann, M. de Wild, Tailoring Selective Laser Melting Process Parameters for NiTi Implants, J. Mater. Eng. Perform. 21 (2012) 2519-2524.

[36] K. Otsuka, X. Ren, Physical metallurgy of Ti–Ni-based shape memory alloys, Prog. Mater. Sci 50 (2005) 511-678.

[37] J. Frenzel, Z. Zhang, C. Somsen, K. Neuking, G. Eggeler, Influence of carbon on martensitic phase transformations in NiTi shape memory alloys, Acta Materialia 55 (2007) 1331-1341.

[38] X. Wan, Y. Feng, X. Lin, H. Tan, Large superelastic recovery and elastocaloric effect in as-deposited additive manufactured Ni50.8Ti49.2 alloy, Appl. Phys. Lett. 114 (2019).

[39] S. Dadbakhsh, B. Vrancken, J.P. Kruth, J. Luyten, J. Van Humbeeck, Texture and anisotropy in selective laser melting of NiTi alloy, Mater. Sci. Eng., A 650 (2016) 225-232.

[40] R.F. Hamilton, B.A. Bimber, T.A. Palmer, Correlating microstructure and superelasticity of directed energy deposition additive manufactured Ni-rich NiTi alloys, J. Alloys Compd. 739 (2018) 712-722.

[41] N. Shayesteh Moghaddam, S. Saedi, A. Amerinatanzi, A. Hinojos, A. Ramazani,

J. Kundin, M.J. Mills, H. Karaca, M. Elahinia, Achieving superelasticity in additively manufactured NiTi in compression without post-process heat treatment, Sci. Rep. 9 (2019).

[42] S. Dadbakhsh, M. Speirs, J.-P. Kruth, J. Schrooten, J. Luyten, J. Van Humbeeck, Effect of SLM Parameters on Transformation Temperatures of Shape Memory Nickel Titanium Parts, Adv. Eng. Mater. 16 (2014) 1140-1146.

[43] S. Kumar S, L. Marandi, V.K. Balla, S. Bysakh, D. Piorunek, G. Eggeler, M. Das, I. Sen, Microstructure – Property correlations for additively manufactured NiTi based shape memory alloys, Materialia 8 (2019).

[44] R.F. Hamilton, B.A. Bimber, M. Taheri Andani, M. Elahinia, Multi-scale shape memory effect recovery in NiTi alloys additive manufactured by selective laser melting and laser directed energy deposition, J. Mater. Process. Technol. 250 (2017) 55-64.

[45] H. Halim, D.S. Wilkinson, M. Niewczas, The Portevin–Le Chatelier (PLC) effect and shear band formation in an AA5754 alloy, Acta Materialia 55 (2007) 4151-4160.